PHYSICAL REVIEW E **94**, 063303 (2016)

Mass-flow-rate-controlled fluid flow in nanochannels by particle insertion and deletion

Paul L. Barclay[*] and Jennifer R. Lukes[†]
Department of Mechanical Engineering and Applied Mechanics, University of Pennsylvania,
Philadelphia, Pennsylvania 19104, United States

(Received 5 August 2016; revised manuscript received 5 October 2016; published 2 December 2016)

A nonequilibrium molecular dynamics method to induce fluid flow in nanochannels, the insertion-deletion method (IDM), is introduced. IDM inserts and deletes particles within distinct regions in the domain, creating locally high and low pressures. The benefits of IDM are that it directly controls a physically meaningful quantity, the mass flow rate, allows for pressure and density gradients to develop in the direction of flow, and permits treatment of complex aperiodic geometries. Validation of IDM is performed, yielding good agreement with the analytical solution of Poiseuille flow in a planar channel. Comparison of IDM to existing methods indicates that it is best suited for gases, both because it intrinsically accounts for compressibility effects on the flow and because the computational cost of particle insertion is lowest for low-density fluids.

DOI: 10.1103/PhysRevE.94.063303

I. INTRODUCTION

With potential impacts in a wide variety of fields from medicine and biotechnology to robotics and avionics, micro- and nanoscale liquid and gas flows have become increasingly important in recent years [1–14]. Devices such as pacemakers [1], nanoprobes [4], nanosensors [10,11], nanopumps [6,10], and nanoturbines [10] and processes such as drug delivery [3], desalination [7], and shale gas extraction [13,14] involve flows at small scales. Having a complete understanding of such flows could reduce drag [15], wear [16], and leakage [9] of micro- and nanomachinery, while allowing for better thermal management and control [1,2] of these devices and processes.

Pressure-driven flow is an important flow regime for nanochannels [12,17], carbon nanotubes [5], and nanopipettes [18]. Molecular dynamics (MD) simulation [19] has been widely used to study nanoscale flow in these [3,16,20] and other systems [7]. It has been shown in MD studies that continuum Poiseuille flow descriptions, which assume constant fluid properties, no-slip boundaries, and a constant pressure gradient $\partial P/\partial x$ along the length of a fluid channel, are valid down to the nanometer scale if appropriate interactions between the walls and fluid are used [21,22] and if fluid properties are adjusted to account for confinement effects [16,20]. The horizontal velocity, u, and mass flow rate, $\dot{m}$, in Poiseuille flow are given by [23]

$$u(y) = \frac{3\dot{m}}{2\rho_B L_y L_z}\left(1 - \frac{4y^2}{L_y^2}\right), \tag{1a}$$

$$\dot{m} = -\frac{\rho_B L_y^3 L_z}{12\mu}\frac{\partial P}{\partial x}. \tag{1b}$$

In Eqs. (1a) and (1b), y is the direction perpendicular to the wall, ρ_B and μ are the bulk density and bulk viscosity of the fluid, L_y is the channel height with walls located at $\pm L_y/2$, and L_z is the channel depth.

Several methods have been developed to induce planar Poiseuille flow in MD [24–39]. The most commonly used technique is the body force method (BFM) [24]. BFM applies an external body force, f, to all fluid atoms in order to induce flow. Typically a constant force is applied (BFM-C). Recently, a BFM based on constraint dynamics has been developed [25]. Termed Gaussian dynamics by the authors and here as BFM-GD, the method maintains a desired momentum and thus controls the mass flow rate in the system. The benefits of BFMs are the simplicity of implementation, the wide range of accessible flow regimes [40], and a simple physical understanding of what is happening to each fluid particle. A drawback of BFMs, arising from their application to periodic systems, is that pressure gradients do not arise directly in the simulations. The pressure can be corrected by removing the hydrostatic portion due to f,

$$P_{\text{corr}} = P - \frac{\rho_B f}{m}(x - x_0), \tag{2}$$

where m and x_0 are the particle mass and zero reference frame for the force field and P is the internal fluid pressure,

$$P = \rho k_B T + \frac{1}{3V}\sum_{i\neq j}^{N} \mathbf{r}_{ij}\cdot\mathbf{F}_{ij}(\mathbf{r}_{ij}). \tag{3}$$

Here $\rho, k_B, T, V, N, \mathbf{r}_{ij}$, and $\mathbf{F}_{ij}$ are the number density, Boltzmann constant, temperature, volume of the region, number of particles, displacement between particles, and interaction force between particles. For incompressible or nearly incompressible fluids, this correction is valid and yields a pressure gradient in the flow direction of magnitude $\rho_B f/m$. However, its validity for compressible fluids is questionable. Another drawback of BFMs is that the body force needed for flow to develop on computationally accessible time scales is quite large [36].

Dual control volume grand canonical molecular dynamics (DCV-GCMD) [26,41–45] is another method that has been used to drive flow. This method uses grand canonical Monte Carlo (GCMC) to select particle configurations that maintain different chemical potentials in control volumes at either end of the flow domain, and alternates GCMC with MD moves that advances particle positions (both inside the control volumes

---

[*] pbarc@seas.upenn.edu

[†] Corresponding author: jrlukes@seas.upenn.edu

and between the control volumes). The benefit of DCV-GCMD method is that it allows precise setting of the fluid properties in the GCMC control volumes [41,42]. The main drawback is that it requires several GCMC moves for every MD move, which becomes computationally expensive as the pressure [46] or density [36] increases.

In this paper we develop an MD method, the insertion-deletion method (IDM), to induce fluid flow in nanochannels. IDM addresses drawbacks of the techniques above and allows control of the mass flow rate, a physically relevant quantity. A description of IDM is provided in Sec. II. In Secs. III A and III B, mass flow rates, viscosities, and velocity, pressure, and density profiles from IDM are compared to those from the analytical Poiseuille flow solution and to BFM and DCV-GCMD. This comparison shows that IDM produces the expected fluid flow characteristics and highlights the advantages of IDM, as compared to other methods, for modeling flows where fluid compressibility effects are important. Section III C compares the computational efficiencies of IDM, BFM, and DCV-GCMD. Section III D discusses details of the kinetic and potential energies computed in IDM and shows that energy fluctuations induced by the method are two orders of magnitude smaller than those arising from the thermostat. Finally, Sec. IV presents conclusions and future directions.

II. METHOD

A. IDM description

IDM controls the mass flow rate by inserting and deleting particles in distinct regions of the simulation domain. Figure 1 shows a schematic of the IDM: Ω_I and Ω_D represent the regions where particles are inserted and deleted. The inserted particles create a high pressure in the center of the domain while the deleted particles create a low pressure near the edges. This causes symmetric pressure gradients and therefore symmetric flow profiles to develop, as indicated by the arrows in Fig. 1. Ω_I and Ω_D can be regarded as particle sources and sinks, respectively, while Ω_S represents the region where the fluid is steadily flowing. The general algorithm for IDM is as follows: (a) insert k particles in Ω_I and delete k particles in Ω_D, (b) run MD for n steps, (c) repeat. The set mass flow rate is

$$\dot{m}_{\text{set}} = \frac{km}{n\Delta t}, \tag{4}$$

where Δt is the time step chosen for the simulation. Due to the symmetry of the system, half of the mass is expected to flow in the positive x direction with the other half flowing in the negative x direction. In most other methods to induce Poiseuille flow, the mass flow rate is a dependent quantity driven by external forces, fictitious membranes [27], physical pistons [28–31], or boundary regions that establish pressure [32], chemical potential [26,41–45], or temperature [38] gradients. IDM and BFM-GD directly control the mass flow rate, leaving other variables, namely pressure and density, as dependent quantities.

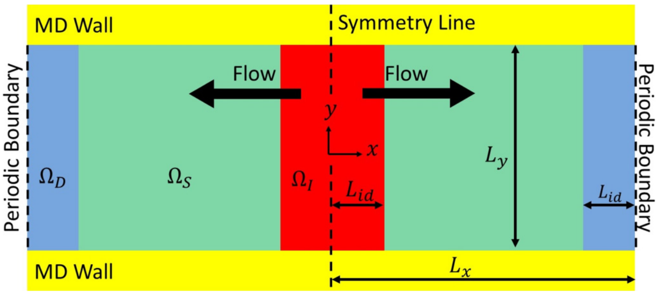

FIG. 1. IDM schematic. Particles are inserted in Ω_I (red), deleted in Ω_D (blue), and flowing in Ω_S (green).

B. IDM implementation

The dimensionless truncated and shifted Lennard-Jones potential [19],

$$\phi(r_{ij}) = \begin{cases} 4\epsilon_{ij}\left(\frac{1}{r_{ij}^{12}} - \frac{1}{r_{ij}^{6}} - \frac{1}{r_c^{12}} + \frac{1}{r_c^{6}}\right) & \text{if } r_{ij} \leqslant r_c \\ 0 & \text{else,} \end{cases} \tag{5}$$

where ϵ_{ij} and r_c are the potential well depth and the cutoff radius, is used for all interactions. The parameters used for the fluid-fluid, wall-wall, and fluid-wall interactions and cutoff radius are $\epsilon_{\text{FF}} = 1$, $\epsilon_{\text{WW}} = 9$, $\epsilon_{\text{FW}} = 0.75$, and $r_c = 2.5$ in order to mimic the no-slip boundary condition [47]. The walls are modeled by four layers of particles in an FCC lattice. The position of the outermost layer is fixed in space in order to contain the system while the inner three layers are permitted to move based upon the above interactions. The velocity Verlet algorithm is used with a time step $\Delta t = 0.005$. Periodic boundary conditions are applied in length, x, and depth, z, directions. The height of the channel is $L_y = 17.18$ and length of the insertion region is $L_{\text{id}} = 2.56$. Other dimensions, densities, and temperatures are given in Table I for the high- and low-density fluids ("liquid" and "gas," respectively) modeled in this work. All quantities are expressed in Lennard-Jones reduced units.

The fluid particles and wall particles are initialized in an FCC lattice. The mobile wall and fluid particles are initialized with a temperature of $T = 0.001T_{\text{set}}$. The temperature is then ramped to T_{set} over 50000 steps in order to melt the fluid lattice. Next, the system is held at T_{set} for 100 000 steps before IDM is started. Particles are then inserted via the USHER algorithm [48] in Ω_I and deleted from random locations in Ω_D at various rates (Table I). The USHER algorithm finds an insertion location such that the potential energy of the inserted particle is within a set tolerance, here ±5% unless otherwise noted, of a desired potential energy. USHER initially chooses a random starting location in Ω_I, which is iteratively updated

TABLE I. Parameters for the four IDM cases modeled.

					$k = 1$		$k = 2$	
	ρ	T_{set}	L_x	L_z	n	$\dot{m}_{\text{set}}$	n	$\dot{m}_{\text{set}}$
Liquid 1	0.757	0.8	41.04	30.78	2–25	8–100	4–25	16–100
Liquid 2	0.757	0.8	82.08	30.78	5	40	–	–
Liquid 3	0.757	0.8	123.12	30.78	5	40	–	–
Gas	0.074	1.2	41.04	51.30	4–25	8–50	–	–

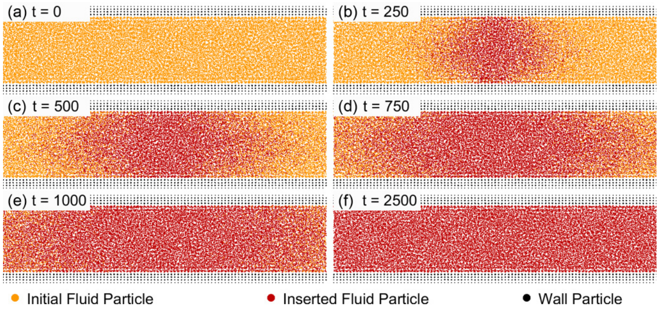

FIG. 2. Snapshots of particle positions at various times for the liquid system with $\dot{m}_{\mathrm{set}} = 40$.

via a Newton-Raphson method until the targeted potential energy, here the instantaneous average potential energy per particle in Ω_I before insertion, is achieved. The velocity of the inserted particles is chosen from the Maxwellian distribution corresponding to the instantaneous temperature in Ω_I. IDM is then run using LAMMPS [49] for at least 100 000 steps to collect statistics.

Velocity rescaling thermostats are used to control temperature [19]. Temperatures are calculated using the thermal velocities, $\mathbf{v}_i^{(T)} = \mathbf{v}_i - \mathbf{v}_{\mathrm{ave}}$ where $\mathbf{v}_i$ and $\mathbf{v}_{\mathrm{ave}}$ are the velocity of particle i and the average velocity of the thermostatted region. Separate thermostats were used for insertion (Ω_I), deletion (Ω_D), leftward flowing (Ω_S,$x < 0$), and rightward flowing (Ω_S,$x > 0$) regions, which is similar to the thermostatting techniques used in DCV-GCMD methods [50].

III. RESULTS AND DISCUSSION

A. IDM consistency checks

To verify that IDM produces physically meaningful flow, various checks of the method were performed. First, simulations were run and snapshots of the particle positions were taken at various times (Fig. 2). The startup time was found to be short, with the system reaching a steady state in approximately 50 time units (10 000 time steps). As the flow developed, the inserted (dark red) particles displayed a spatial distribution consistent with the expected parabolic profile [Eq. (1a)] and a clear left-right symmetry with respect to the insertion region. Next, local temperature profiles were evaluated and found to be roughly constant throughout the entire domain, as expected. As an additional check, the instantaneous distribution of the particle velocity components within the central region of Ω_S (away from Ω_I, Ω_D, and the walls) was computed and found to be well fit by the Maxwell-Boltzmann distribution for T_{set}. Finally, the mass flow rate actually produced in IDM simulations was compared to the set mass flow rate in Eq. (4). This was done by counting the number of particles crossing the middle of Ω_S and computing the actual mass flow rate from this value. Excellent agreement between $\dot{m}_{\mathrm{set}}$ and the MD mass flow rate (Fig. 3) was found for both liquid and gas flows.

B. IDM validation and comparison

Next, velocity, density, and pressure profiles generated by IDM were compared to the analytical solution for Poiseuille flow [Eq. (1a)] and to results from BFM-C, BFM-GD, and DCV-GCMD methods. Details of our implementation of these methods are given in the Appendix. Figure 4 shows the number density and horizontal velocity in the center of Ω_S for typical liquid and gas simulations. The density profiles of all methods are the same for both liquid and gas. The center of the channel has the bulk density, and the fluctuating densities near the walls are indicative of the expected solid-like layers that arise from atomic ordering [51]. The liquid simulations produce parabolic velocity profiles that are very well represented by the theoretical profile of Eq. (1a), which includes no fitting parameters. At the wall, the velocity goes to zero, indicating that the liquid does not slip at the surface. The velocity profiles for the gas are well fit by the parabolic profile if Eq. (1a) is adjusted to include gas slip [52] at the walls.

Figure 5 shows the normalized number density and pressure along the length of the channel in Ω_S with $L_x = 41.04$. In all cases shown, BFM-C and BFM-GD density and pressure profiles are indistinguishable. For the liquid, the IDM density and pressure profiles are very similar to the BFM profiles [Figs. 5(a) and 5(c)], with differences less than 2% [Figs. 6(a) and 6(b), $L_x = 41.04$] at all positions within Ω_S. In contrast, the IDM profiles for the gas are markedly different from the BFM profiles. These differences arise from the periodic boundary conditions used in BFM, which do not permit development of density gradients in the fluid. The assumption of constant fluid density is reasonable for liquids, as is shown in Fig. 5(a) by the close agreement between IDM and BFM, but is questionable for gases [Fig. 5(b)], where compressibility effects become important. This is also manifested in the pressure profiles shown in Figs. 5(c) and 5(d). The hydrostatic-corrected [Eq. (2)] BFM pressure profiles, which assume a constant density, match well with IDM for the liquid but show

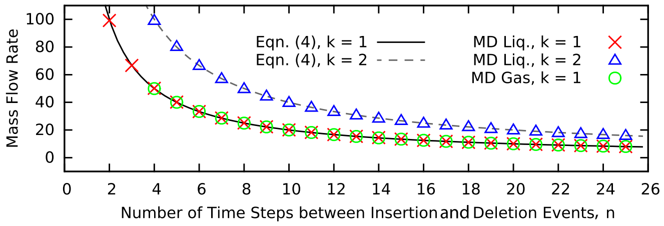

FIG. 3. Mass flow rate versus number of steps between insertion and deletion events. An event refers to the insertion and deletion of k particles in Ω_I and Ω_D, respectively. Standard error is smaller than marker size.

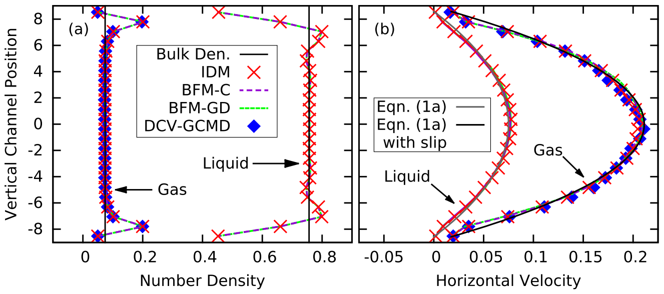

FIG. 4. (a) Number density and (b) horizontal velocity versus vertical channel position for $L_x = 41.04$. The mass flow rate for the liquid is $\dot{m}_{\mathrm{set}} = 40$ while the mass flow rate for the gas is $\dot{m}_{\mathrm{set}} = 20$.

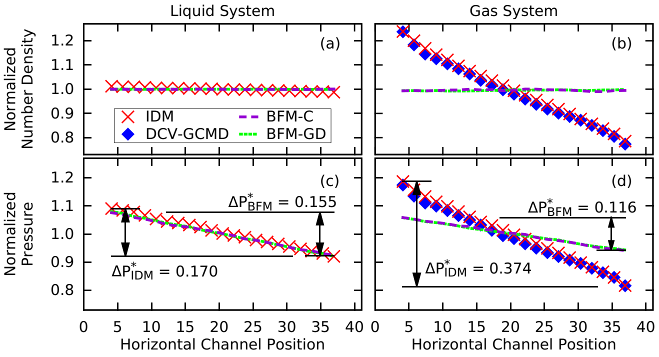

FIG. 5. (a, b) Normalized number density and (c, d) normalized pressure versus horizontal channel position for $L_x = 41.04$. The density is normalized by the bulk density and the pressure is normalized by the BFM-C pressure before the hydrostatic portion is removed. The mass flow rate for the liquid (a, c) is $\dot{m}_{\text{set}} = 40$, while the mass flow rate for the gas (b, d) is $\dot{m}_{\text{set}} = 20$.

pronounced differences for the gas. DCV-GCMD simulations were also run for the gas and show good agreement with IDM. This agreement lends confidence that IDM produces physically meaningful results and indicates that differences between IDM and BFM likely result from the artificially flat density profile enforced in BFM.

The limitations of the constant density assumption in BFM do not show up exclusively in gaseous systems. Even for liquid systems, this assumption begins to lose validity as the channels become longer. Figure 6 shows the percent differences in density and pressure between IDM and BFM-C as a function of channel position for three channel lengths. Larger differences indicate that larger errors are being introduced by the constant density assumption. For all three channel lengths, the density differences are smallest in the middle of Ω_S (normalized channel position 0.5), and largest near Ω_I and Ω_D (normalized positions of 0 and 1, respectively). As channel length increases, these differences become more pronounced, with the longest channel ($L_x = 123.12$) having a difference of ±4% [Fig. 6(a)]. Similar differences are observed for the pressure profiles [Fig. 6(b)]. It is important to note that the longest channels, which display the largest differences between IDM and BFM density and pressure profiles, also experience the highest drops in pressure across Ω_S for a constant mass flow rate [Eq. (1b)]. The normalized pressure drop, $\Delta P^* = \Delta P / P_0$, for the smallest channel is 0.170 for IDM and 0.155 for the BFMs (Fig. 5). IDM has a pressure drop that is 0.015 (9.7%) higher than the BFMs for the shortest channel [Fig. 5(c)] and 0.055 (12.0%) higher for the longest channel. These differences in ΔP^* are fairly significant for the liquid but are much smaller than the increases seen by the gas with IDM being 0.26 (223%) higher and 0.68 (237%) higher then BFM for $\dot{m} = 20$ and $\dot{m} = 50$, respectively. These results imply that, for compressible fluids, BFMs can significantly underestimate the pressure drops required to induce flow at a given mass rate. Based on these observations we recommend that BFM only be applied to nearly incompressible systems.

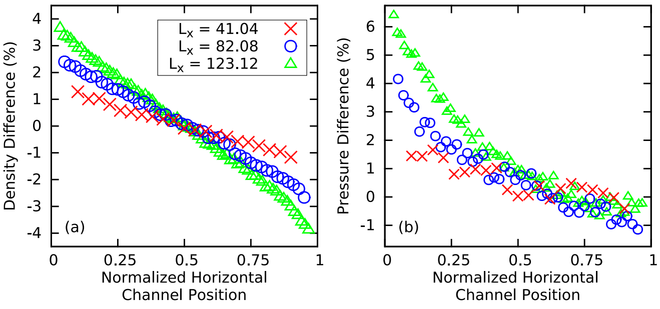

FIG. 6. Percentage difference in (a) density and (b) pressure between IDM and BFM-C versus normalized horizontal channel position for the liquid. The mass flow rate is $\dot{m}_{\text{set}} = 40$.

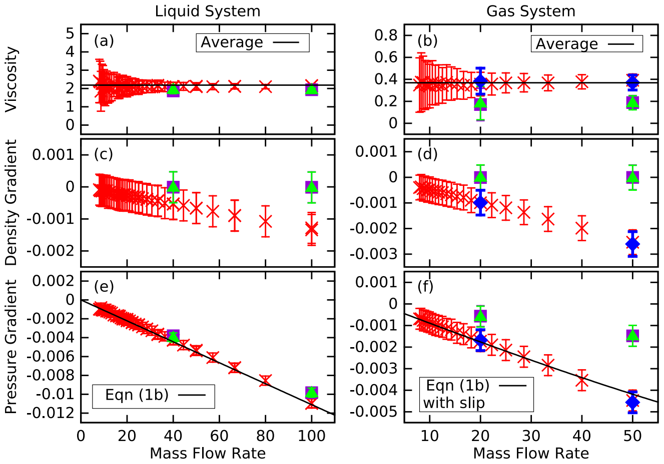

FIG. 7. (a, b) Viscosity, (c, d) density gradient, and (e, f) pressure gradient versus set mass flow rate for the (a, c, e) liquid and (b, d, f) gas systems. The "×," "■," "▲," and "◆" markers represent IDM, BFM-C, BFM-GD, and DCV-GCMD, respectively.

Using Eqs. (1b) and (4), an effective viscosity for the channel can be obtained from linear pressure fits and the set mass flow rate. Figures 7(a) and 7(b) show that the viscosity for the various liquid and gas cases is roughly constant and is similar in magnitude to values found in the literature [16,27,37,53]. Due to underestimation of the pressure gradient in BFM-C and BFM-GD for the gas, the viscosity calculated by these methods is noticeably lower than that of IDM and DCV-GCMD (a similar result is true for the liquid case but the difference is difficult to notice).

Figures 7(c)–7(f) show the IDM, BFM-C, BFM-GD, and DCV-GCMD density and pressure gradients obtained for various mass flow rates set in Eq. (4). IDM shows excellent agreement with Eq. (1b) and with DCV-GCMD, indicating that it can successfully model a range of mass flow rates. In contrast, BFM-C and BFM-GD show notable deviations from these benchmarks, with worse agreement at higher mass flow rates. Equation (1b) in Figs. 7(e) and 7(f) is calculated from the weighted average viscosity and bulk density (note that it is adjusted in the gas to account for fluid slip). The error bars in Fig. 7 represent the uncertainty in the slope of the pressure (or density) fit.

C. Computational cost

Although IDM and DCV-GCMD allow for density and pressure gradients to develop in a flow, these gradients come at

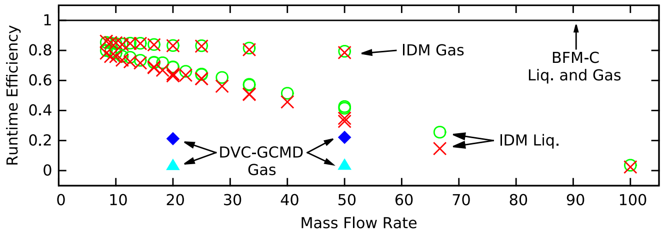

FIG. 8. Runtime efficiency, defined as BFM-C runtime divided by IDM (or DCV-GCMD) runtime, for simulations of 10 000 time steps. The “×” and “○” are IDM simulations with USHER acceptance criteria of 5% and 10%, respectively. The “♦” and “▲” are DVC-GCMD simulations with 75 and 686 GCMC steps for every MD step, respectively.

an increased computational cost compared to BFM. Figure 8 shows the computational efficiency of IDM and DCV-GCMD when run on four 3.0 GHz Intel Xeon Processors each with 2.00 GB RAM. The run times for BFM-C (normalizing factor) are roughly constant as expected because a larger mass flow rate requires a larger applied force which does not require any excess computation. The run times for BFM-GD (not shown) are comparable with the run times of BFM-C. For IDM, however, an increased mass flow rate requires USHER to be called more frequently which, for liquids, significantly increases the computational cost. Additionally, as the mass flow rate increases the density gradient increases [Figs. 7(c) and 7(d)], leading to higher densities in Ω_I that decrease the efficiency of USHER [48]. The increasing computational cost is less noticeable for the gas because even for the largest mass flow rate Ω_I still has a large number of potential insertion locations. The acceptance criterion of USHER also plays a part in the computational time required. Changing USHER's acceptance criterion from 5% to 10% had minimal impact on the flow, with the velocity, density, and pressure profiles being similar in both cases. Additionally, the difference in runtime between the two cases is minimal, especially when compared to BFM-C runtimes. For the gas the IDM computational cost is about 25% greater than that of BFM-C for all simulated mass flow rates.

Although IDM is computationally more expensive than BFM-C, it is almost four times less expensive than DCV-GCMD with a ratio of 75 GCMC attempts for every MD time step. If the number of GCMC moves is increased to 686 (this number was chosen to follow the standard practice [19,54] that the number of GCMC translation attempts is roughly the number of particles in Ω_I or Ω_D) then IDM becomes 25 times less computationally expensive than DCV-GCMC. The computational cost of DCV-GCMD increases with density and pressure [36,46] due to the increased computational cost of calculating the energy change for a GCMC attempt as well as the increased number of GCMC steps needed to maintain the desired chemical potential. For this reason, DCV-GCMD simulations were not run for liquid systems.

D. Energy of inserted and deleted particles

For a given insertion or deletion event, IDM can add energy to or remove energy from the domain because the inserted and deleted particles are not required to have the same energy. It is thus interesting to examine what effect such events have on the energies in Ω_I and Ω_D. Figures 9(a) and 9(b) show the potential and kinetic energy distributions of the inserted and deleted liquid particles for two mass flow rates: $\dot{m}_{\rm set} = 20$ [Fig. 9(a)] and $\dot{m}_{\rm set} = 40$ [Fig. 9(b)]. In each figure, the kinetic energy distributions of inserted and deleted particles are almost identical, which confirms that the temperatures in Ω_I and Ω_D are similar (as expected due to the thermostats). In contrast, the potential energy distributions of inserted and deleted particles are different, displaying sharp and broad peaks, respectively. The broad potential energy distribution of the deleted particles indicates that the particles are indeed being removed randomly. As expected, the average potential energy of deleted particles $\langle \phi_D \rangle$ matches the average background potential energy per particle in the deletion region $\langle \phi_{\Omega_D} \rangle$; agreement within about 1% is found (Table II). In this table, the percentage difference is defined $(\langle \phi_D \rangle - \langle \phi_{\Omega_D} \rangle)/|\langle \phi_{\Omega_D} \rangle|$. The approximately 13% error bar on this difference arises from the broad distribution of deleted particles shown in Fig. 9.

TABLE II. Density, average potential energy of inserted (deleted) particles, and percentage difference from the background potential energy in insertion (deletion) region for IDM runs corresponding to Fig. 9.

			Insertion			Deletion		
k	n	$\dot{m}_{\rm set}$	ρ	$\langle \phi_I \rangle$	% Diff.	ρ	$\langle \phi_D \rangle$	% Diff.
1	10	20	0.768	−4.45	4.82 ± 1.22	0.744	−4.53	0.68 ± 13.56
2	20	20	0.768	−4.45	4.81 ± 1.24	0.744	−4.56	0.02 ± 13.36
1	5	40	0.778	−4.51	4.81 ± 1.18	0.731	−4.44	1.16 ± 13.95
2	10	40	0.778	−4.51	4.85 ± 1.18	0.732	−4.48	0.28 ± 13.80

The sharp potential energy distribution of the inserted particles arises from the acceptance criteria of USHER. When USHER inserts a particle, it finds a location such that the inserted particle's potential energy matches the average per particle potential energy in Ω_I. Consistent with the USHER tolerance of ±5%, Table II shows that the inserted particles' average potential energy is about 4.8% higher than the

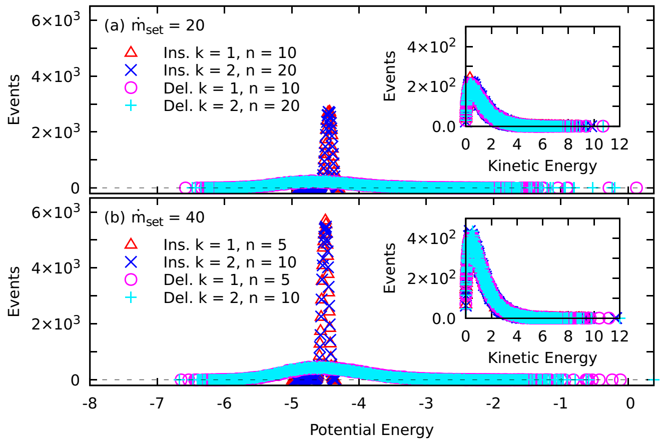

FIG. 9. Potential and kinetic (inset) energy distributions of inserted and deleted particles for (a) $\dot{m}_{\rm set} = 20$ and (b) $\dot{m}_{\rm set} = 40$ for the liquid system. One event refers to inserting or deleting one particle.

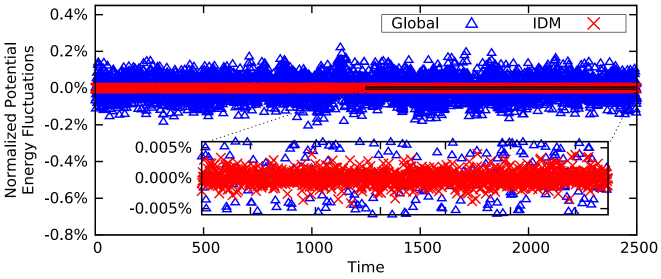

FIG. 10. Normalized potential energy fluctuations for $\dot{m}_{\text{set}} = 40$ for the entire liquid domain, △, and due to IDM, ×. The inset shows a finer resolution.

background potential energy in the insertion region, $\langle \phi_I \rangle$. This difference could be reduced by tightening the tolerance, at the cost of increased computational time due to additional required iterations.

Simulations at different flow rates [Figs. 9(a) and 9(b) and Table II] reveal several key features. First, for a fixed value of $\dot{m}_{\text{set}}$, the potential energy distributions are insensitive to the specific values chosen for k and n. Second, as expected, the number of insertion or deletion events doubles as the flow rate doubles. Third, and more subtly, the potential energy peak positions shift with mass flow rate. The inserted particle peak shifts to lower potential energy with increased mass flow rate, and the deleted particle peak shifts to higher potential energy. The differences between the potential energy peak locations for different $\dot{m}_{\text{set}}$ values stem from the corresponding density differences in Ω_I and Ω_D (Table II). An increased density in Ω_I implies that the average particle spacing in Ω_I decreases, which in turn implies that the fluid particles are further down the Lennard-Jones potential well. On average, this should result in a lower potential energy per particle. Similar reasoning can be used to explain the inverse trend for Ω_D.

As the inserted and deleted particles have different potential energy distributions (Fig. 9), it is important to know the magnitudes of any energy imbalances that may result and compare these to the global energy flucuations of the entire liquid domain that are induced by thermostatting. Figure 10 shows the instantaneous net potential energy addition due to IDM, defined as potential energy of inserted particles minus potential energy of deleted particles, and also the instantaneous global potential energy. Both are normalized by the global average dimensionless potential energy, -149169, calculated during the last 400 000 time steps (2000 time units) of the simulation for a liquid domain at $\dot{m}_{\text{set}} = 40$ ($k = 1$ and $n = 5$). The potential energy fluctuations of the entire domain are small ($\approx 0.2\%$) and those due to the IDM are two orders of magnitude smaller than the global fluctuations. Since the kinetic energy differences of the inserted and deleted particles have already been shown to be negligible (inset of Fig. 9), it is found that any instantaneous energy imbalances induced by IDM are dwarfed by those induced by thermostatting.

IV. CONCLUSIONS

A method to induce planar Poiseuille flow in molecular simulations, IDM, has been developed. The method allows for direct control of a physically meaningful quantity, the mass flow rate. Insertion of particles in the central region and deletion of particles at the edges creates a pressure difference that induces flow. The pressure varies linearly along the length of the channel, as expected from continuum assumptions, when the temperature of the system is properly controlled and when the fluid is dense. The velocity profile is parabolic and the mass flow rate and pressure gradient also match continuum predictions when the fluid viscosity is adjusted to account for confinement effects. For liquid flows through short channels, IDM and BFM methods yield similar density and pressure profiles when a hydrostatic correction is made to BFM pressure. For gas flows, IDM and DCV-GCMD profiles agree well with each other but not with those from BFM. The differences in profiles arise from compressibility effects, which are accounted for in IDM and DCV-GCMD but not in BFM.

Advantages of IDM over existing methods to induce Poiseuille flow include its ability to handle compressibility effects and nonuniform pressure gradients, its adaptability to arbitrarily complex geometries, and its reduced computational cost relative to DCV-GCMD. If the fluid of interest has negligible compressibility and a simple flow geometry, BFM methods are preferable due to their significantly lower computational cost. For gases, however, compressibility effects are significant and the IDM is preferable because it captures these effects with minimal additional computational cost.

ACKNOWLEDGMENT

Support from the Department of Education GAANN Grant No. P200A120237 is greatly appreciated.

APPENDIX: BFM-C, BFM-GD, AND DCV-GCMD IMPLEMENTATION

This appendix describes pertinent implementation details of the BFM-C, BFM-GD, and DCV-GCMD methods that have been compared to IDM. For BFM-C, the constant applied body force, f, was calculated by combining Eqs. (1b) and (2) and using the known viscosity of the system, which was found using the method described in Sec. III B. The initial velocity in BFM-GD was set such that $u_{\text{ave}} = \dot{m}_{\text{set}}/(\rho_B L_y L_z)$. The similarity between BFM-C and BFM-GD found in Sec. III B is expected because the values computed for f in BFM-C and $\langle f \rangle$ in BFM-GD were found to be the same within error.

For DCV-GCMD, Ω_I and Ω_D were used as the control volumes. The chemical potential was set to maintain a similar bulk density and mass flow rate. The values for the chemical potentials were found by trial and error, and for $\dot{m} \approx 20$ the values were -13.16 in Ω_I and -14.10 in Ω_D, and for $\dot{m} \approx 50$ the values were -13.06 and -17.27, respectively. The ratio of GCMC moves to MD time steps need to be such that the chemical potential in the desired region is maintained. Based upon the literature [26,41–45] a ratio of 75 to 1 was used with two-thirds of the GCMC moves being particle translation attempts and one-third of the GCMC moves being insertion or deletion attempts. These values ensured that the mass flow rate and bulk density were within 3% of the desired values.

[1] A. Rostami, A. Mujumdar, and N. Saniei, Int. J. Heat Mass Transf. **38**, 359 (2002).

[2] C. Neto, D. R. Evans, E. Bonaccurso, H.-J. Butt, and V. S. Craig, Rep. Prog. Phys. **68**, 2859 (2005).

[3] Y. Li, J. Xu, and D. Li, Microfluidics Nanofluidics **9**, 1011 (2010).

[4] B. Bourlon, J. Wong, C. Mikó, L. Forró, and M. Bockrath, Nature Nanotechnol. **2**, 104 (2007).

[5] M. Whitby and N. Quirke, Nature Nanotechnol. **2**, 87 (2007).

[6] G. M. Whitesides, Nature **442**, 368 (2006).

[7] A. Aghigh, V. Alizadeh, H. Wong, M. S. Islam, N. Amin, and M. Zaman, Desalination **365**, 389 (2015).

[8] S. A. Saadati and E. Roohi, Aerospace Sci. Technol. **46**, 236 (2015).

[9] Y. Qi, X. Meng, D. Mu, Y. Sun, and H. Zhang, Energy **102**, 252 (2016).

[10] O. Ejtehadi, E. Roohi, and J. A. Esfahani, Intl. Commun. Heat Mass Transfer **39**, 439 (2012).

[11] R. Yoo, J. Kim, M.-J. Song, W. Lee, and J. S. Noh, SensorsActuators B: Chem. **209**, 444 (2015).

[12] Q. Wu, J. T. Ok, Y. Sun, S. Retterer, K. B. Neeves, X. Yin, B. Bai, and Y. Ma, Lab Chip **13**, 1165 (2013).

[13] C. Guo, J. Xu, K. Wu, M. Wei, and S. Liu, Fuel **143**, 107 (2015).

[14] L. Geng, G. Li, P. Zitha, S. Tian, M. Sheng, and X. Fan, Fuel **181**, 887 (2016).

[15] A. Busse, N. D. Sandham, G. McHale, and M. I. Newton, J. Fluid Mech. **727**, 488 (2013).

[16] Y.-z. Hu, H. Wang, Y. Guo, and L.-q. Zheng, Wear **196**, 243 (1996).

[17] E. Tamaki, A. Hibara, H.-B. Kim, M. Tokeshi, and T. Kitamori, J. Chromatogr. A **1137**, 256 (2006).

[18] M. G. Schrlau, E. M. Falls, B. L. Ziober, and H. H. Bau, Nanotechnology **19**, 015101 (2008).

[19] D. Frenkel and B. Smit, *Understanding Molecular Simulation: From Algorithms to Applications*, Vol. 1 (Academic Press, San Diego, 2001).

[20] J. A. Thomas and A. J. McGaughey, Nano Lett. **8**, 2788 (2008).

[21] C. Liu and Z. Li, Phys. Rev. E **80**, 036302 (2009).

[22] C. Liu and Z. Li, AIP Adv. **1**, 032108 (2011).

[23] B. R. Munson, D. F. Young, and T. H. Okiishi, *Fundamentals of Fluid Mechanics* (Wiley, New York, 2009).

[24] J. Koplik, J. R. Banavar, and J. F. Willemsen, Phys. Rev. Lett. **60**, 1282 (1988).

[25] S. E. Strong and J. D. Eaves, J. Phys. Chem. Lett. **7**, 1907 (2016).

[26] G. S. Heffelfinger and F. van Swol, J. Chem. Phys. **100**, 7548 (1994).

[27] J. Li, D. Liao, and S. Yip, Phys. Rev. E **57**, 7259 (1998).

[28] M. Sun and C. Ebner, Phys. Rev. A **46**, 4813 (1992).

[29] C. Huang, K. Nandakumar, P. Y. Choi, and L. W. Kostiuk, J. Chem. Phys. **124**, 234701 (2006).

[30] H. Takaba, Y. Onumata, and S.-i. Nakao, J. Chem. Phys. **127**, 054703 (2007).

[31] L. Wang, R. S. Dumont, and J. M. Dickson, J. Chem. Phys. **138**, 124701 (2013).

[32] W. D. Nicholls, M. K. Borg, D. A. Lockerby, and J. M. Reese, Microfluidics Nanofluidics **12**, 257 (2012).

[33] F. Zhu, E. Tajkhorshid, and K. Schulten, Biophys. J. **83**, 154 (2002).

[34] E. G. Flekkøy, R. Delgado-Buscalioni, and P. V. Coveney, Phys. Rev. E **72**, 026703 (2005).

[35] E. Flekkøy, G. Wagner, and J. Feder, Europhys. Lett. **52**, 271 (2000).

[36] I. Hanasaki and A. Nakatani, Modell. Simul. Mater. Sci. Eng. **14**, S9 (2006).

[37] Z. Zhang, H. Zhang, and H. Ye, Appl. Phys. Lett. **95**, 154101 (2009).

[38] Q. D. To, T. T. Pham, G. Lauriat, and C. Léonard, Adv. Mech. Eng. **4**, 580763 (2012).

[39] A. Kalra, S. Garde, and G. Hummer, Proc. Natl. Acad. Sci. U.S.A. **100**, 10175 (2003).

[40] N. V. Priezjev, Phys. Rev. E **75**, 051605 (2007).

[41] J. R. Bordin, J. S. Andrade Jr, A. Diehl, and M. C. Barbosa, J. Chem. Phys. **140**, 194504 (2014).

[42] J. Zheng, E. M. Lennon, H.-K. Tsao, Y.-J. Sheng, and S. Jiang, J. Chem. Phys. **122**, 214702 (2005).

[43] Y. Lü and M. Chen, Nanotechnology **19**, 215707 (2008).

[44] T. Mutat, J. Adler, and M. Sheintuch, J. Chem. Phys. **136**, 234902 (2012).

[45] G. Arya, H.-C. Chang, and E. J. Maginn, J. Chem. Phys. **115**, 8112 (2001).

[46] K. Chae and L. Huang, J. Phys. Chem. B **119**, 12299 (2015).

[47] I. A. Cosden and J. R. Lukes, Comput. Phys. Commun. **184**, 1958 (2013).

[48] R. Delgado-Buscalioni and P. Coveney, J. Chem. Phys. **119**, 978 (2003).

[49] S. Plimpton, J. Comput. Phys. **117**, 1 (1995).

[50] N. K. Kanellopoulos, *Recent Advances in Gas Separation by Microporous Ceramic Membranes*, Vol. 6 (Elsevier, New York, 2000).

[51] S. Toxvaerd, J. Chem. Phys. **74**, 1998 (1981).

[52] P. A. Thompson and S. M. Troian, Nature **389**, 360 (1997).

[53] J. Haile, *Molecular Dynamics Simulation*, Vol. 18 (Wiley, New York, 1992).

[54] LAMMPS, http://lammps.sandia.gov/ (Sandia Corporation, 2013), accessed on September 16, 2016.